IEEE Access
Multidisciplinary | Rapid Review | Open Access Journal

Received 7 March 2025, accepted 22 March 2025, date of publication 26 March 2025, date of current version 4 April 2025.

Digital Object Identifier 10.1109/ACCESS.2025.3555140

RESEARCH ARTICLE

In-Depth Analysis of Ka-Band Integrated Commercial Beamformer Non-Idealities in Phased Array Calibration and Pattern Prediction Methods for 5G Scenarios

JORGE CALATAYUD MAESO[1], (Graduate Student Member, IEEE), XIAOLIANG SUN[1], ALFONSO TOMÁS MURIEL-BARRADO[2], FERNANDO RODRIGUEZ VARELA[3], PABLO SÁNCHEZ-OLIVARES[1], JOSÉ-MANUEL FERNÁNDEZ-GONZÁLEZ[1], (Senior Member, IEEE), AND MANUEL SIERRA CASTAÑER[1], (Fellow, IEEE)

[1]Information Processing and Telecommunications Center, ETSI Telecomunicación, Universidad Politécnica de Madrid, 28040 Madrid, Spain
[2]Group of Radio Frequency: Circuits, Antennas and Systems (RFCAS), Escuela Politécnica Superior, Universidad Autónoma de Madrid, 28049 Madrid, Spain
[3]Department of Signal Theory and Communications and Telematic Systems and Computing Group of Microwave Engineering and Radiocommunication Systems, Universidad Rey Juan Carlos, 28032 Madrid, Spain

Corresponding author: Jorge Calatayud Maeso (jorge.cmaeso@upm.es)

This work was supported by Spanish Government, Ministry of Economy, National Program of Research, Development and Innovation under the Project New Array Antenna Technologies and Digital Processing for the FUTURE Integrated Terrestrial and Space-Based Millimeter Wave Radio Systems—Universidad Politecnica de Madrid (UPM)-InTerSpaCE—Proyecto financiado por Ministerio de Ciencia e Innovación (MCIN)/Agencia Estatal de Investigación (AEI)/10.13039/501100011033 under Grant PID2020-112545RB-C51.

ABSTRACT This paper comprehensively examines the non-idealities inherent in commercially available beamformers and explores their implications in the calibration procedures for phased array antennas. The non-ideal nature of the beamformer is meticulously modeled and assessed through extensive S-Parameter measurements to discern its impact on analyzed excitation retrieval methods. The Rotating-element Electric-field Vector (REV) and Control Circuit Encoding (CCE) methods are simulated using a synthetic array with spherical wave expansion driven by output coefficients measured from the beamformer. Simulations are executed to compare the REV method with a Selective-REV variant, designed to enhance coefficient prediction accuracy by leveraging a priori knowledge of phase-shifter amplitude deviations. Additionally, amplitude, phase, and complex CCE encodings are employed to determine the encoding technique that best accommodates beamformer non-idealities. Finally, anechoic chamber measurements assess the pattern prediction capabilities of the analyzed methods, and an iterative calibration scheme is proposed to compensate for the studied beamformer errors due to its behavior.

INDEX TERMS Integrated circuits, active phased arrays, calibration, pattern estimation, antenna integrated circuit, antenna measurements, peripheral probe calibration.

I. INTRODUCTION

Millimeter-Wave (mm-Wave) technology is playing a crucial role in the fifth generation of cellular systems (5G), offering the potential for high data rates due to the substantial bandwidth available in the mm-Wave band [1]. This technology is particularly promising for achieving gigabit/s throughput in wireless communication links, as it can be employed for multi-gigabit/s outdoor transmission. This includes serving as directional links for wireless backhaul and access technology for transmissions between base stations (BSs) and Mobile Stations (MSs) as part of 5G research initiatives. However, mm-Wave signals face challenges such as high path loss due to their extremely high carrier frequencies. Several state-of-the-art projects from the European Space Agency (ESA) are implementing

The associate editor coordinating the review of this manuscript and approving it for publication was Shah Nawaz Burokur.

reconfigurable platforms for communications systems in Ka-band that overcome these limits using reconfigurable antenna schemes [2], [3], [4].

To mitigate these challenges and ensure reasonable signal-to-noise ratios, high-gain antennas are essential. Antenna arrays with adaptive beamforming become crucial, especially in scenarios where the propagation channel may change [5], [6], [7] over time. These array antennas can be subdivided into multiple small arrays to satisfy an adaptive resource allocation [8]. However, large active phased array antennas can have enormous power consumption requirements if beamforming is performed digitally, similarly to how it is currently used on the lower bands. Adaptive beamforming helps to focus the signal using directive and electronically reconfigurable beams [9]. Determining the optimal beam direction in mm-wave adaptive arrays can be complex, often requiring an exhaustive search through its possible directions [10]. To minimize power consumption, high-integrated IC-based analog beamforming is an alternative for reconfiguring the antenna radiation pattern.

Analog beamformers operating in millimeter wave bands suffer from many non-idealities, such as amplitude variations induced by the selected phase setting or interchannel coupling [11], [12], [13], [14], [15], [16], [17]. Accurate evaluation and diagnosis of these errors in phased array antennas is essential. It is even more relevant when the proposed architecture relies on multiple smaller arrays instead of a larger array. Thus, diagnosing and mitigating the amplitude and phase errors of the beamformer becomes even more crucial. Additional errors induced by the degradation of the RF components over time should also be able to be measured. These non-idealities directly affect the beamforming procedure and, therefore, the reconfigurability performance of the system. These ICs may show additional non-linearities (gain linearity, intermodulation products…) that may be meaningful from an application perspective and can induce severe signal degradation. However, these effects are usually compensated by the signal source as the beamforming does not have any mechanism to correct these non-linearities. [18], [19], [20] Due to the high volume of millimeter wave systems deployed, offline calibration may be economically unfeasible, so establishing on-site diagnosis models and methods may be the only choice to prolong the life cycle of this equipment.

Phased array calibration methods allow the extraction of the excitation coefficient of all the array elements for a given array configuration. Knowing the approximate excitation of each element is particularly useful for highly reconfigurable antennas since it allows one to make reliable estimations of the array patterns without directly measuring them. Phased array calibration methods can be classified into 4 different categories. First, one of the most common calibration methods is the mutual coupling method [21], [22], [23]. However, this method requires the capability to transmit and receive simultaneously. A second approach consists of installing a coupled network [24] that allows us to extract a sample of the signal sent by the antenna and calibrate the array in real time. This method is unfeasible for many millimeter-wave architectures because of space constraints. Some beamformers provide some self-calibration monitoring system [17]. However, in commercial beamformers, these monitors only measure amplitude data. Usually, the measured data do not have enough resolution to perform a reasonable adjustment. Third, the park and probe method [25] is extensively used for near-field calibration. The field radiated by the array is measured by a moving probe at a distance of 3λ to 5λ. This technique is time-consuming and impossible to perform on-site or online. Finally, the peripheral probe methods have two main strategies for retrieving the excitation coefficients of the array. First, the Rotating-element Electric-field Vector (REV) method [26], [27], [28] retrieves the excitation of the array coefficients by sweeping through the phase-shifter states. Alternatively, Control Circuit Encoding (CCE) consists of measuring the signal radiated by the phased array configured following an orthogonal coding matrix as stated in [29] and [30] and then decoding the array excitation coefficient from the probe received signal.

This work aims to extensively study the non-idealities of commercial beamformers by modeling all the error contributions of the array excitation coefficients in Section II. Based on this study, extensive research of the most fitting calibration methods is performed to estimate how these non-idealities affect pattern estimations in Section III. A Selective-REV method is also proposed to improve the calibration performance by considering the non-idealities of the beamformer under test. Alternative multiple CCE encoding matrices are also studied to evaluate their performance with the beamformer errors. The goal of testing multiple calibration schemes is to validate the accuracy of these calibration schemes at mm-wave bands with highly integrated circuity since most of the previous studys are performed at lower frequency bands [29], [31], [32], [33]. The validation of the simulations provided in Section III is carried out in the anechoic chamber in Section IV, where a pattern prediction comparison using the studied phased array excitation extraction methods is done. Finally, an iterative correction procedure of the array excitation coefficients has been performed.

II. NON-IDEAL BEHAVIOUR OF HIGHLY INTEGRATED BEAMFORMERS

Planar phased array antennas at mm-wave bands have really tight space constraints to place their circuitry [34], [35], [36]. Therefore, it is key to integrate as many components of the RF chain into this small available space as possible. One of the most successful commercial state-of-the-art solutions for a transmit beamformer is based on the integration of eight independently controllable RF front-ends formed by a common VGA (Variable Gain Amplifier) amplifier to compensate for signal splitting and amplitude and phase

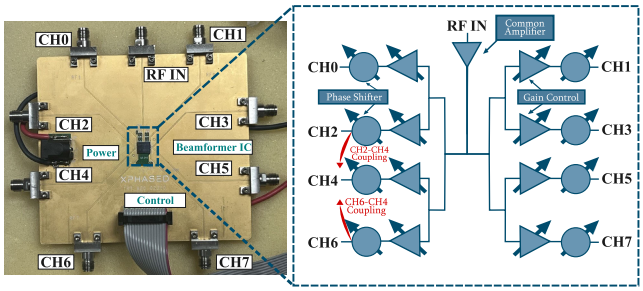

FIGURE 1. Beamformer evaluation board and internal signal path diagram.

control for each branch based on a 4 to 6 bit phase shifter and attenuator with an independent amplifier [12], [13], [14], [15]. The architecture illustrated in Fig. 1 shows the general diagram for a commercial beamformer from the Xphased brand with a 6-bit phase shifter and 30 dB attenuation control with 0.5 dB jumps. This beamformer chip configuration allows feeding four array elements by a single IC in an electrically reconfigurable polarization scheme or eight array elements without polarization control, leaving enough space between the ICs to route the distribution network among several beamformers and the common port.

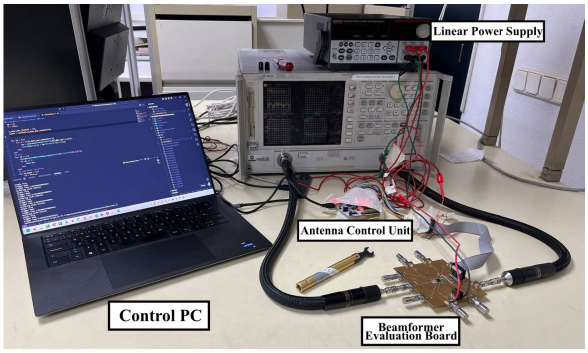

FIGURE 2. Test setup for validation of the behavior model of the output coefficients of the commercial beamformer.

Ideally, the complex output coefficient (V_i) for the i-th channel of the beamformer should follow Eq. 1, where α_i and β_i are the programmed amplitude and phase bit-states for the i-th channel, ΔA and $\Delta\phi$ are the phased and amplitude control increments. This implies that the amplitude and phase functions (A_i and Φ_i) only depend on the amplitude and phase bit-state respectively.

$$V_i = A_i(\alpha_i)e^{j\Phi_i(\beta_i)} = (\alpha_i \Delta A)e^{j\beta_i \Delta\phi} \tag{1}$$

However, as stated in [11], and measured using the setup shown in Fig. 2, there is an amplitude mismatch on the channel under test when the phase bits of that channel are modified as shown in Fig. 3. This first non-ideality is due to the variance in the phase shift loss and is intrinsic to the MMIC phase shifter architectures [37], [38], [39]. However, the relative phase change is very accurate, as illustrated in Fig. 4. The measured Root Mean Squared (RMS) error of the relative phase shift is 2.51 degrees. The exposed beam transforms Eq.1 into Eq. 2 where the term $A_i(\alpha_i)$ now depends on the phase bit β_i of that channel. The phase term can remain as in the ideal model since the error is quantitatively low.

$$V_i = A_i(\alpha_i, \beta_i)e^{j\beta_i \Delta\phi} \tag{2}$$

Furthermore, when the amplitude of a given channel is measured while sweeping the phase bits of an adjacent channel, an amplitude mismatch is recorded, as shown in Fig. 3. This amplitude variation, with a sine-like shape, is due to internal coupling between channels on the beamformer and represents an additional contribution to the array excitation coefficient. To model the behavior of beamformers, taking into account all the error sources of the final output coefficient, Eq. 3 is proposed. The Eq. 3 adds a coupling term in the form of a sum of the contribution of the interfering channels. The intensity of the coupling is modeled by the term C_n, which depends on the configured amplitude bit of the interfering channel.

$$V_i = A_i(\alpha_i, \beta_i)e^{j\beta_i \Delta\phi} + \sum_{\substack{n=1 \\ n\neq i}}^{N} C_n(\alpha_n)e^{j\beta_n \Delta\phi} \tag{3}$$

Eq. 3 has been verified with measurements of the S-Parameters of an evaluation board of a commercial beamformer with the setup shown in Fig. 2.

This equation models all error sources that distort the desired coefficient, such as the amplitude disturbance induced by the phase shifter state $A_i(\alpha_i, \beta_i)$. The error is shown in Fig. 3 as the amplitude of the channel whose phase is swept does not remain constant, and its variance shows dependence on its phase state. This amplitude variance is common across multiple commercial and novel research beamformers in mm-Wave bands due to its phase shifter architecture [37], [38], [39]. However, the relative phase jump of a channel can be modeled as ideal as the measurements shown in Fig. 4. A coupling term has been added to model the interchannel coupling inside the IC. Not all channels of the IC are coupled in the same manner. In the evaluated beamformer, these channels depend on the state of the channel itself.

For the beamformer under test, the coupling terms can be simplified to the contribution of only one / two adjacent channels following the distribution shown in Fig. 1. This effect is also illustrated in Fig. 3. It can be seen that the amplitude of CH2 changes when the phase shifter of that channel is swept and when the phase of the other channels is also swept. Phase shifting the channels physically adjacent to CH2 (CH0, CH4, and CH6) generates a more significant amplitude variation than performing the same action for those on the opposite side of the beamformer (CH1, CH3, CH5, and CH7). Also, the shape of the opposite channels remains very similar among them despite the phase variation of the channel

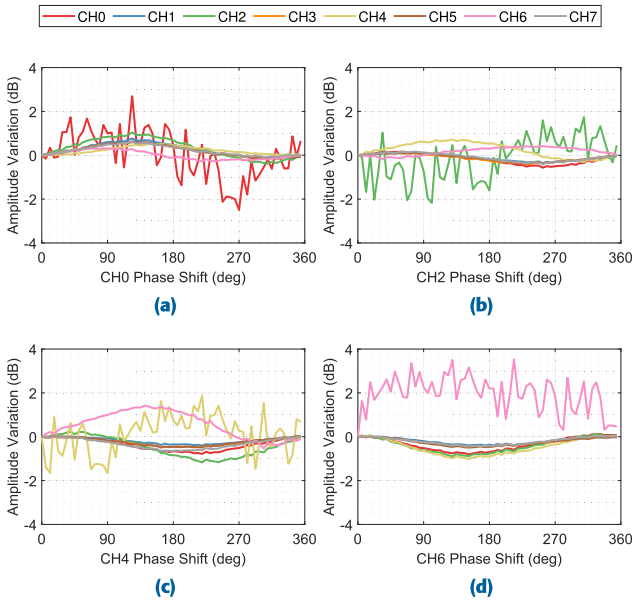

FIGURE 3. Amplitude variation induced when the phase shifter of the channel [(a) CH0 (b) CH2 (c) CH4 (d) CH6] is swept at 28 GHz.

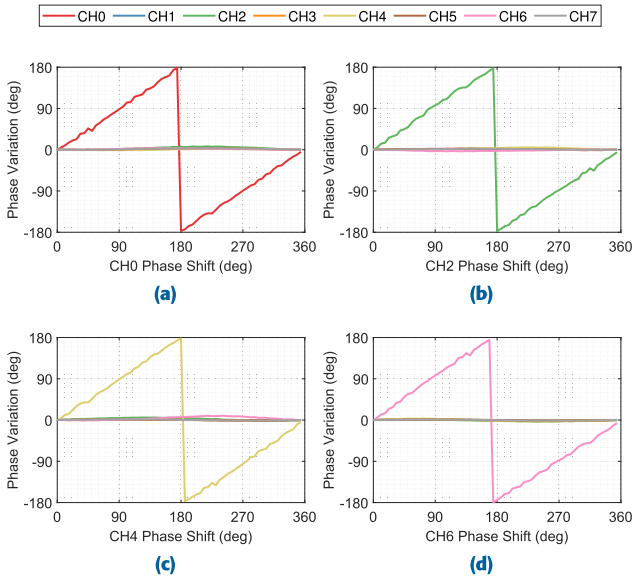

FIGURE 4. Phase variation when the phase shifter of the channel [(a) CH0 (b) CH2 (c) CH4 (d) CH6] is swept at 28 GHz.

that is being swept. For the latter configuration, the amplitude variation of CH2 exhibits a sine-like shape, showing that there is a coupling between those adjacent channels. By filtering the high-frequency ripple measured in Fig. 3 for different phase states on the adjacent channels and fitting the result data into multiple sine curves a ± 1.3 dB amplitude variation due to interchannel coupling has been estimated. To further investigate the coupling effect, broadband measurements have been carried out over CH2 to check how it can be disturbed. Fig. 5 shows the amplitude and phase distortion induced in CH2 by all the other channels of the beamformer along several CH2 phase states, showing the worst-case perturbation range. This interchannel coupling effect remains significant across the entire operating frequency band.

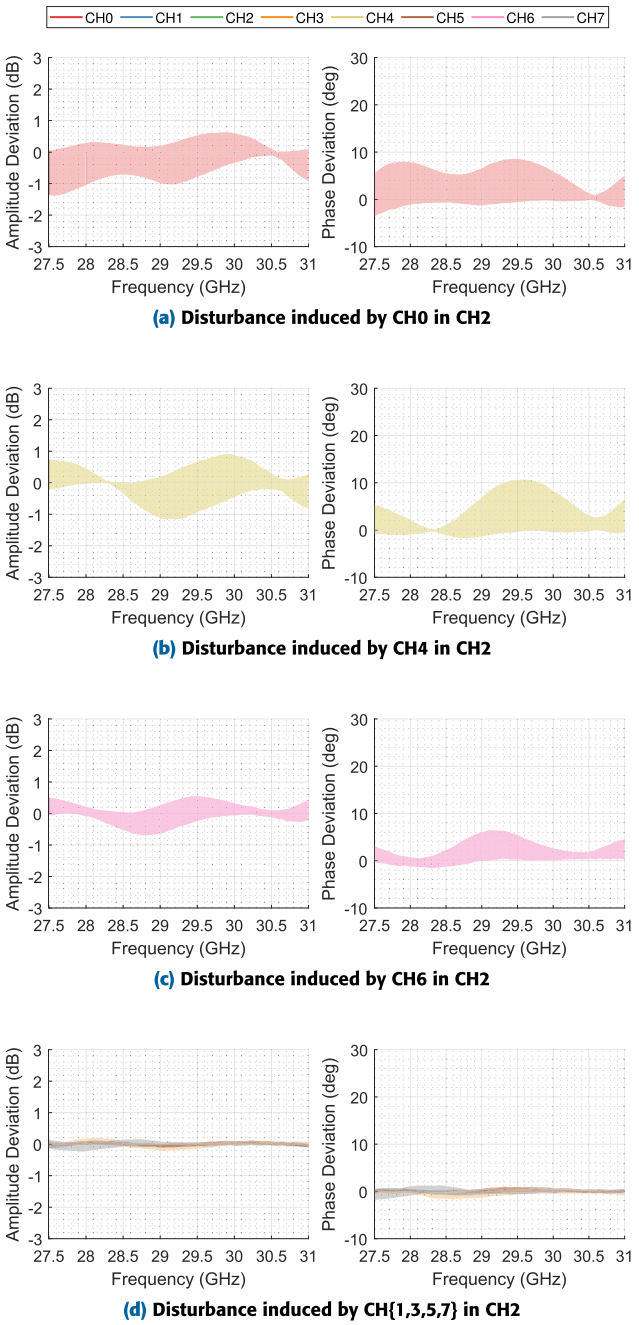

FIGURE 5. Amplitude and phase deviations distribution over frequency for measured in CH2 when the phase state of the remaining channels is swept.

This coupling also generates a floor effect when the value A_i is small. In high-attenuation configurations, the desired output signal level is not achieved if the nearby channels are not also attenuated, since the coupling term is larger than

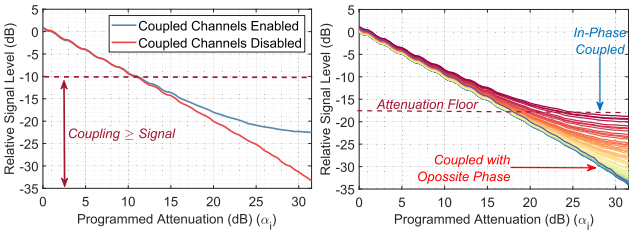

FIGURE 6. Signal attenuation measured when (a) coupled channels are turned on/off (b) the channel under measure modify its phase.

the channel signal contribution. This effect was measured in Fig. 6. If only the channel under measurement is turned on, the whole relative 30 dB attenuation range is achieved, as shown in Fig. 6a. However, there is a clear difference in the attenuation level achieved when the coupled channels are switched ON, generating the floor effect. On the one hand, Fig. 6b shows that the internal coupling is responsible for the floor effect. On the other hand, this floor level depends on the phase of the current channel, as shown in Fig. 6b.

Finally, the coupling effect is not only an error but also a constraint on making assumptions about the chip's behavior. Each output coefficient is dependent not only on its channel configuration but also on its neighbor states. This completely eliminates the possibility of calibrating each channel independently.

This study of the coupling effects has been performed in a narrow band perspective since most currently in-use satellite and 5G applications use less than 500 MHz for Satellite Communications [40], [41] and 400 MHz for 5G FR2 operation [1] instantaneous bandwidths. Fig. 5, shows the frequency response of the amplitude and phase variation of CH2 induced by all the phase configurations of the other beamformer channels. While the envelope of the curve remains constant across the whole frequency range, it can be expected that the coupling behavior is not the same for all frequencies. The biggest discrepancy occurs at 30.5 GHz, where the coupling behavior is heavily reduced for a 300 MHz band. The worst phase deviation for the frequency range (27.5 GHz to 31 GHz) is less than 10 degrees. Meanwhile, the amplitude discrepancy across the whole band is within 0.7 dB. Since many applications will use narrower instantaneous bandwidths, it can be stated that the single frequency approximation made for studying the coupling behavior is valid.

III. APPLICATION OF CALIBRATION METHODS TO MM-WAVE BEAMFORMERS

A. SELECTION BETWEEN THE DIFFERENT CALIBRATION METHODS FOR AN ACTIVE PHASED ARRAY

The main limitation the beamformer induces when calibrating a phased array is the interaction between each channel configuration. The inability to analyze the behavior of each channel independently wholly eliminates the possibility of using park-and-probe methods for calibration. Finally, peripheral probe methods, based on some signal encoding, allow the extraction of the excitation coefficient of a given element when the rest of the elements are in their operating condition. This enables the opportunity to calibrate each element considering the contribution of the interchannel coupling coming from the beamformer. However, the amplitude variance generated by phase changes induces additional errors when decoding the received signals by the probe.

Peripheral probe methods have two main strategies for retrieving the excitation coefficients of the array. The first one is the REV method [26]. The second one cosists on solving a linear equation system based on some orthogonal code [29], [30] using the circuitry of the phased array (Control Circuit Encoding) to represent the symbols of an encoding matrix, generally Hadamard matrices [42]. The whole diagram of the usual peripheral probe methods is shown in Fig. 7. It must be remarked that these methods are based on modifying the excitation under test (a_i) with some prior knowledge that is assumed to be ideal (Encoding provided by the H matrix). This is a known phase shift in the REV method or an encoding quantity for the orthogonal encoding. The signal emitted by the array in all the required configurations is measured by a probe (b_m) and then decoded back to retrieve an estimation of the actual array excitation coefficients.

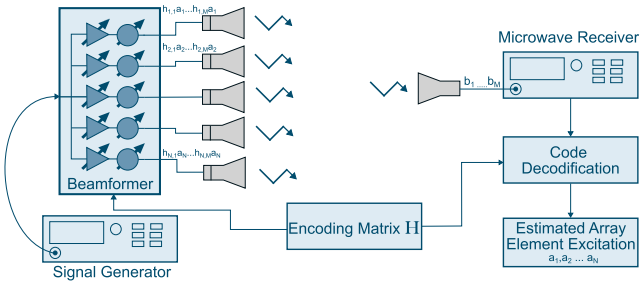

FIGURE 7. Measurement setup for peripheral probe calibration methods.

B. THE REV METHOD

The Rotating-element Electric-field Vector (REV) method is an array excitation extraction method based on the superposition of the fields radiated by each element that resembles the array [26]. The total field radiated by an array of N elements in a given configuration ($\vec{E}_{array}$), in a given state of its circuitry, can be written as Eq. 4, where the i-th element on the array is the selected element to perform the REV method. If an additional phase term ($\phi_i(\beta_i)$) is added to the field radiated by the element under test for a certain value of $\phi_i(\beta_i)$ the amplitude of $\vec{E}_{array}$ will be maximum ($\vec{E}_{max}$) or minimum ($\vec{E}_{min}$). To check for which value of ($\phi_i(\beta_i)$) total array field ($\vec{E}_{array}$) satisfies the last condition, the phase

shifter of the i-th channel is swept.

$$\vec{E}_{array} = \vec{E}_i + \sum_{\substack{n=1 \\ n\neq i}}^{N} \vec{E}_n = \vec{E}_i e^{j\phi_i(\beta_i)} + \sum_{\substack{n=1 \\ n\neq i}}^{N} \vec{E}_n \tag{4}$$

To retrieve the amplitude and phase excitation of the array element under test Eq. 5 and Eq. 6 are used. In this equations $\Gamma = \frac{|\vec{E}_{max}|+|\vec{E}_{min}|}{|\vec{E}_{max}|-|\vec{E}_{min}|}$ and Δ_0 is the phase-shift required to achieve $\vec{E}_{max}$. This process has to be done for each array element. Since Eq. 4 has to exhibit a sine-like behavior when β_i is swept for a 360-degree phase shift; theoretically, only four equally spaced phase-shifts are required to fit the parameters of a sinusoidal curve accurately. However, in many applications, the precision of the method increases when additional samples are used in the fitting to filter noise and reflections. There is an ambiguity in retrieving the excitation coefficients using Eq. 5 and Eq. 6 depending if the total phase displacement of $\vec{E}_{array}$ is less than 180 degrees or not. This phase ambiguity can be solved by the means explained on [26] and [28]. For some scenarios, the REV method can be performed phaseless, making it ideal for its implementation in on-site calibration since measurement can be performed with more cost-effective power detectors. Since the REV method has to be performed for each element of the array, improvements have been done by grouping elements as in [27]. However, the assumptions made in these improved versions of the REV method cannot be ensured when working with the non-idealities of the beamformers.

$$K = \begin{cases} \dfrac{\Gamma}{1+2\Gamma cos(\Delta_0)+\Gamma^2}, & \text{if } \Phi(\vec{E}_{array}) < 180 \\ \dfrac{1}{1+2\Gamma cos(\Delta_0)+\Gamma^2}, & \text{if } \Phi(\vec{E}_{array}) \geq 180 \end{cases} \tag{5}$$

$$X = \begin{cases} tan^{-1}(\dfrac{sin(\Delta_0)}{cos(\Delta_0)+\Gamma}), & \text{if } \Phi(\vec{E}_{array}) < 180 \\ tan^{-1}(\dfrac{sin(\Delta_0)}{cos(\Delta_0)+1/\Gamma}), & \text{if } \Phi(\vec{E}_{array}) \geq 180 \end{cases} \tag{6}$$

C. SELECTIVE REV: ADAPTING THE REV METHOD TO THE BEAMFORMER LIMITATIONS

Working with the analyzed beamformer, the degradation of the performance of this method comes from the amplitude variation of the channel whose phase is being swept and the interchannel coupling. Additionally, the total power radiated by the static channels is modified with more predictable behavior, as shown in Fig. 3, where the coupled output amplitude varies following a sinusoidal form. Predicting and correcting these effects on a highly integrated array is not feasible. Previous studies in the literature show models to predict the accuracy of the REV method from the phase and amplitude deviations [43]. However, they assume that the phase and amplitude errors are unrelated. This condition does not apply to the beamformer case since, as shown in Section II, there is a cross dependance between amplitude and phase mismatches.

For the channel under test amplitude variation, there are two possible ways to compensate for this effect. First, the programmable attenuator could correct the amplitude variation in each phase state. However, this modifies the coupling behavior of the adjacent channels, as shown in Eq. 3, so it does not reduce the uncertainty of the method. Secondly, the phase-shifter losses can be measured in radiation to gain knowledge about which phase states have similar amplitude deviations. Only using those samples within an amplitude deviation boundary can improve the sine curve fitting. Since the amplitude variation due to internal coupling is not considered, a good criterion for selecting these points is establishing a boundary of less than ± 0.35 dB amplitude deviation from the initial phase state. Fig. 8 shows the relative amplitude measurement of a beamformer channel without the coupling term. For the initial state, orange dotted points represent those phase states with amplitude variation within the established boundary. From now on, this method will be called *Selective-REV*.

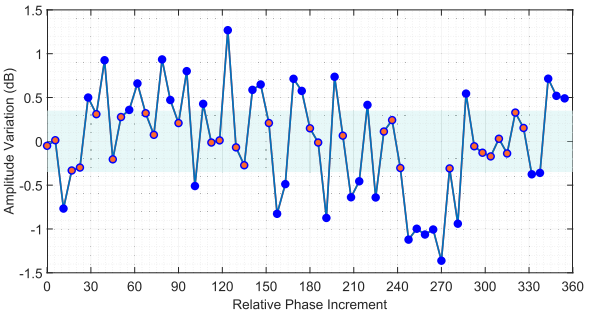

FIGURE 8. Measured amplitude variation for a phase sweep of CH1 with all other channels turned off. Orange dots represent those phase states with an amplitude variation within the established limits.

D. CONTROL CIRCUIT ENCODING CALIBRATION

The relation between the signal received by a probe b positioned in the far-field region of a phased array of N elements can be written as Eq. 7, where a_i and f_i are the excitation coefficient and the pattern of the i-th element of the array. If the probe and array position are kept stationary, Eq. 4 can be written as $b = \sum a_i$. When the array is operating (all elements are radiating simultaneously), the exact individual a_i coefficients are unknown because only its addition can be measured. However, if multiple measurements of b are performed, with a known relative change from the initial values of a_i, a linear equation system can retrieve all a_i values from a set of M measurements of the signal composed by the array. This can be written as Eq. 8, where b represents the measured composed signal of an array radiating with a_i coefficients that are encoded (relatively changed to the initial state) by a matrix H. Using the capabilities of the reconfigurable circuitry of the array to perform a calibration is also called in the literature Control

Circuit Encoding (CCE).

$$b(\theta, \phi) = \sum_{i=1}^{N} a_i f_i(\theta, \phi) \tag{7}$$

$$\mathbf{b} = H\mathbf{a} \tag{8}$$

Solving Eq. 8 relies on choosing a good encoding matrix H. The matrix H should have a low conditioning number and should be easily invertible. Real Hadamard matrices satisfy all these requirements since their conditioning number is 1 and their inverse can be calculated as itself divided by its order [29], [30]. This kind of matrix can be constructed following Eq. 9a and Eq. 9b. However, as stated in Eq. 9, the order of a Hadamard matrix must be 2, or a multiple of 4. Each row and column except the first one are composed of an equal number of +1s and −1s. To ensure the orthogonality of the code, the minimum order of the Hadamard encoding matrix for an array of N elements is set to N+1. If N+1 is not a feasible order for the Hadamard matrix, additional elements with coefficient $a_i = 0$ must be added.

$$H_2 = \begin{bmatrix} 1 & 1 \\ 1 & -1 \end{bmatrix} \tag{9a}$$

$$H_{2^k} = \begin{bmatrix} H_{2^{k-1}} & H_{2^{k-1}} \\ H_{2^{k-1}} & -H_{2^{k-1}} \end{bmatrix} \tag{9b}$$

Traducing the +1's and −1's of the code to physical magnitudes can be done by establishing the rule: If $H_{m,i} = 1$ set the state of that beamformer channel to the original state a_i and if $H_{m,i} = -1$ the state of the beamformer must be set to da_i, where d is the encoding modification. There are multiple strategies to perform the encoding modification d. The most common is to set d to perform a high attenuation or to add a 180-degree phase shift to a_i. This can be conceptually interpreted as the symbols of binary amplitude keying (BAK) or binary phase keying (BPSK) modulations, respectively.

For the beamformer studied, both approaches have similar problems. The amplitude keying according to Eq. 3 modifies the value of the coupling coefficient. On the contrary, the coupled signal is added differently if the phase is shifted. Therefore, due to internal coupling, the orthogonality of the codes will be degraded. Suppose the array is excited with a strong amplitude taper; phase encoding should work better since the attenuation floor measured in Fig. 6 can represent a signal level higher than the required for the −1 state. In contrast, if the amplitude of the array excitation coefficients is set to a similar level, in some cases, the encoding will result in a complete change in the coupling behavior. However, this will only happen for specific values of the initial a_i coefficient, so it will only be a concern for some configurations. The more efficient complex encoding matrix can be found in the literature, [42], [44], [45]. However, using multiple phase states for the encoding severely degrades the performance of the method in analog beamformers due to the amplitude shift induced by the phase changes.

E. SIMULATION OF THE BEAMFORMER CONTRIBUTION TO THE ENCODING ERRORS

To study the contribution of the beamformer to the degradation of the performance of these methods, this work proposes a simulation method based on modeling the signal received by the peripheral probe with the transmission formula from the spherical wave expansion [46]. This tool can be used to consider the degradation introduced by the probe position and orientation and the degradation scenario if desired. Additional effects, such as the ground effect, can be added to perform a more accurate estimate for on-site calibration scenarios [47].

The workflow used to perform this analysis is shown in Fig. 9. Given an ideal desired array, excitation is encoded, generating all the needed beamformer coefficients that should be measured to perform the simulation. These ideal encoded coefficients are then configured in the beamformer. The real excitation coefficients for each encoded configuration the beamformer generates are measured with a VNA. A synthetic phased array (without coupling) is fed by the VNA-measured coefficients containing beamformer errors. The signal the probe would measure for each array configuration in an ideal measurement facility is calculated using the Spherical Wave Expansion (SWE) of the synthetic array generated. Finally, the probe-received signals are decoded using the calibration method under test. This simulation is realistic, as the uncertainty in most calibration methods arises from encoding errors in the beamforming with element coupling at the array level being eliminated. An equivalent noise level of 40 dB and a probe polarisation misalignment of 0.1 degrees is used to replicate anechoic chamber-like conditions.

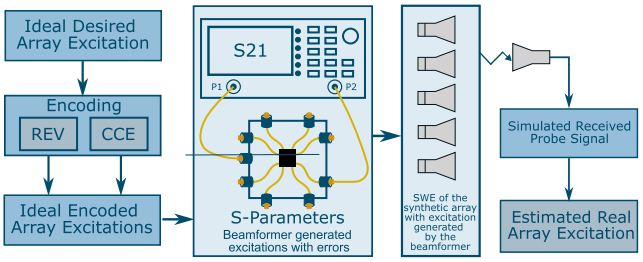

FIGURE 9. Workflow of the proposed simulation method for calculating the probe received signal to simulate the calibration methods.

To remain as close as possible to the capabilities of many spherical near-field antenna ranges, all the simulations performed in this section have been done with a probe-to-array distance of 1m. This is one of the standard distances that most real spherical ranges offer. The synthetic array is a linear array formed by eight uniformly spaced elements at 0.5λ. Two array configurations have been simulated:

1) Broadside Configuration by setting all phase shifters to phase zero and the attenuators to the minimum. (Errors due to the beamformer response are still present)
2) A 20-degree beam steering config by setting a progressive phase-shift of 62 degrees

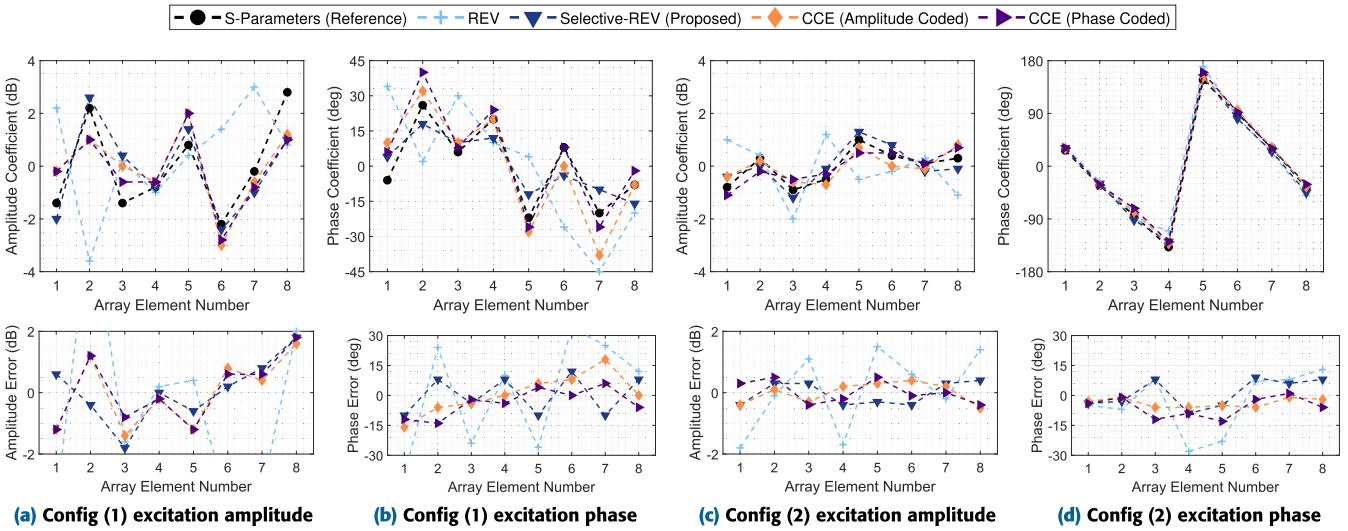

(a) Config (1) excitation amplitude (b) Config (1) excitation phase (c) Config (2) excitation amplitude (d) Config (2) excitation phase

FIGURE 10. Array excitation coefficients retrieved with the proposed simulation method for both configurations (1) beam aiming to broadside with uniform amplitude and (2) beam to 20 degrees with uniform amplitude.

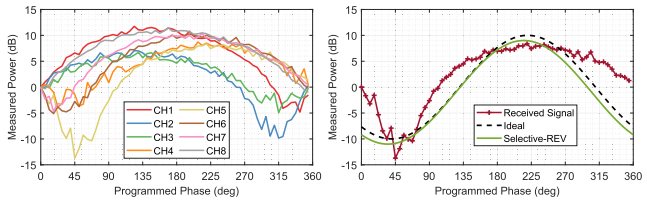

(a) Simulated signals (b) REV sine fitting

FIGURE 11. Comparison of the simulated signal with internal coupling and the ideal case for the REV-Method and Selective-REV sine fitting.

Fig. 10 shows the retrieved excitation coefficients and their error (compared to the VNA measured S-Parameters) in simulation for the two studied scenarios for all the REV and CCE variants under study. As expected, an apparent amplitude mismatch exists between the S-Parameter measurement used as a ground truth value and the traditional REV procedure. However, cleverly selecting which samples are used for the sine interpolation, using the exposed criteria, clearly reduces the amplitude error induced for the configurations simulated. Fig. 11b compares the simulated received signal from the beamformer measurement and the ideally received signal if no amplitude changes were induced by coupling and variance of the phase shifter losses. Observing the simulated received signal by the virtual probe shown in Fig. 11a, the sine shape of the curve is heavily deformed due to changes in the amplitude of each channel. This deformation generates more significant mismatches between the reference coefficients (S-Parameters) and those retrieved by the REV method. The result from the Selective-REV procedure approximates the ideal case.

Comparing the different CCE encoding matrices, both phase and amplitude encodings provide an excellent approximation of the coefficients of the phased array. Amplitude encoding has been done with an attenuation level of 10 dB to the initial state. This attenuation level has been selected so that the signal radiating for each attenuated channel does not wholly interfere with the coupling of the adjacent channels set to the initial state, which has a higher amplitude output. The CCE (Amplitude/Phase) encodings provide accurate results within 1 dB of amplitude and ± 15 degrees in phase as RMS across all elements and configurations. Meanwhile, Selective-REV is able to further improve the accuarcy of the traditional REV but for the broadside scenario, its accuracy is lower than the CCE encoding.

F. PHASED ARRAY PATTERN SIMULATION

These coefficients have been injected into the simulation array model of [11] to better illustrate how the errors affect the simulated coefficients in the final phased array pattern. Fig.12 compares the diagrams generated by the excitation coefficients recovered for both configurations.

The CCE patterns shown in Fig. 12c and Fig. 12d show a similar agreement with the ground truth of the S-parameter as the Selective-REV. For the broadside configuration (Fig. 12c), there is a more significant mismatch on the first right side lobe than in any other angular region of the pattern. For this configuration, the Selective-REV seems to retrieve a better estimation of the whole array pattern. In contrast, the amplitude CCE retrieves an impressive result for the beam-steered configuration. The phase CCE shows a bit of null filling for the side lobes on the right side of the pattern compared to the reference, a symptom of an increased error on the phase terms shown in Fig.10d. For the 20-degree beam steering (Fig. 12b and Fig. 12d), both methods show similar pattern prediction capabilities. The traditional REV method has the most significant SLL error across the pattern. In contrast, Selective-REV shows a better SLL estimation for the left-side secondary lobes, but CCE encodings better retrieve the SLL level on the main beam's right side. However, these inconsistencies are within the uncertainty.

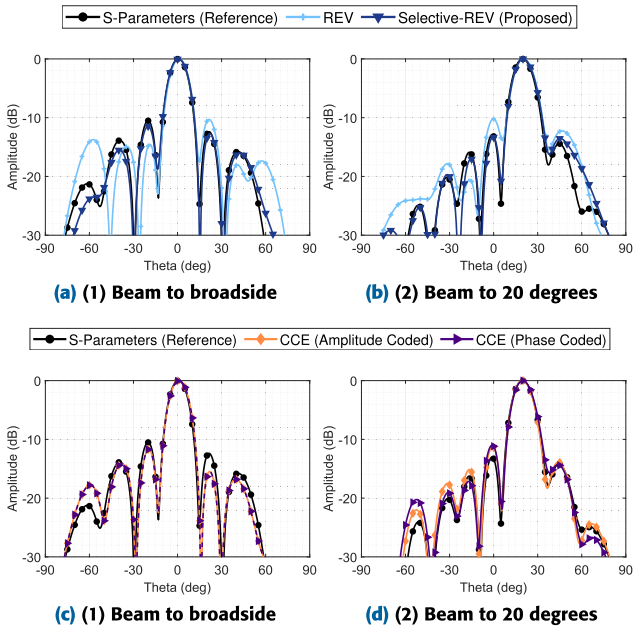

FIGURE 12. Comparison of the simulated diagram using the array coefficients measured in S-Parameters as reference against the estimated phased array patterns from the retrieved excitation coefficients with the calibration methods.

IV. OFFLINE CALIBRATION AND PATTERN PREDICTION IN AN ANECHOIC CHAMBER

A. PATTERN PREDICTION CAPABILITIES

Additional factors can impact the performance of the calibration methods studied in Section III when working with a complete antenna system. Mutual coupling between the radiating elements and electromagnetic interactions of the antenna with fixation elements can severely degrade the performance of the antenna and, therefore, its calibration. Furthermore, in this scenario, the calibration method will not only retrieve the excitation error due to the beamformer mismatch but also consider the mismatch on the distribution network of the antenna. This error should remain constant for each configuration of the beamformer. Additionally, these measurements aim to check if, for a mass production environment, a measurement procedure based on some a priori knowledge of the passive diagrams of the radiating elements and the excitation coefficients extracted by the calibration procedures can give a good estimation of the active diagram without performing a direct diagram measurement.

In order to evaluate the performance of the calibration methods proposed, a measurement campaign of an active phased array was performed on the Spherical Near-Field System (SNF) at UPM's LEHA. The active antenna scheme proposed in [11] was used for this validation. This active antenna is an 8 by 8 column steerable array based on circular patches. The array can steer its beam across the azimuth plane since an independent corporate microstrip network feeds each column. Each column of the array is connected to a different channel of the beamformer IC.

The validation procedure is based on comparing the measurement of the active radiation pattern with a synthetic pattern generated by adding the passive radiation pattern of each array element pondered by the excitation coefficient extracted by the calibration method. Passive radiation patterns were measured by spherical acquisition for each radiating element, connecting a matched load to all remaining elements. Furthermore, in this scenario, the calibration method will not also retrieve the excitation error due to the mismatch of the beamformer-generated excitation coefficients. Still, it will also consider the amplitude and phase mismatch between the different branches of the antenna distribution network. This error term is estimated as almost constant for all configurations and is already present in passive antenna acquisition. Therefore, it should be dembedded from the excitation coefficient retrieved by the calibration method. However, return losses variation in the active element patterns can slightly modify this error term for mid-size arrays [48], [49].

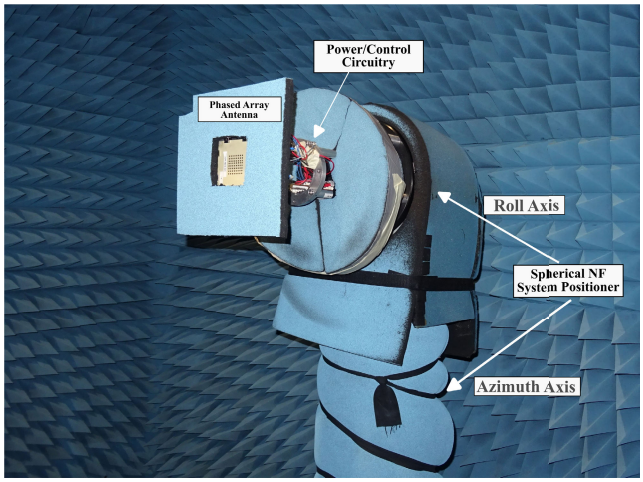

FIGURE 13. Measurement setup for 64 elements active phased array on the LEHA SNF facility.

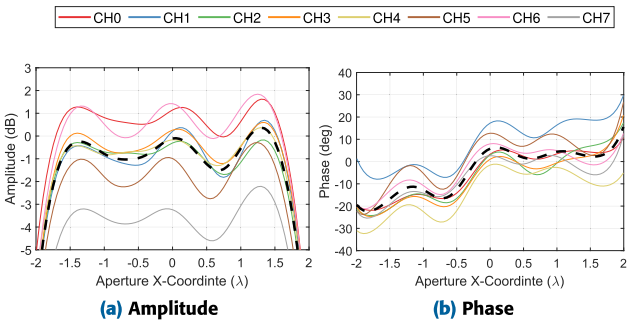

FIGURE 14. Equivalent sources of the ideally combined elements of the phased array, the dotted line represents the average value.

This correction term has been estimated by calculating the equivalent sources for the ideal combined case, which have

been recovered using the relationship between the spherical wave expansion and the plane wave expansion [50], [51]. Since the evaluated array has only beam steering capabilities in the azimuth plane, the antenna and cables' correction coefficient has been extracted by pondering the sources of the eighth array rows and the field for a given patch radius on the excitation dimension. Additionally, for phase correction, the average of the rows was linearly fitted. Fig. 14a and Fig. 14b show the retrieved excitations for each row of the phased array. The differences between each row of the phased array do not matter for the azimuth plane since that imbalance will affect the other plane of the array pattern, whose excitation is set by the distribution network impairments.

To optimize the probe positioning, simulations were conducted using the Monte Carlo method with an equivalent noise level of 40 dB for the signal received by the probe. The main goal of this procedure is to ensure that the probe signal remains as high as possible in all theoretical configurations to be measured. This was especially critical for the CCE-Phase encoding since the resulting encoded pattern from the phase inversion is a difference pattern with a null on the beam steered direction, making inter-comparative measurement results impossible.

The results shown in Fig. 15 correlate with the simulated results for the REV method. As expected, the higher amplitude error recovered by traditional REV shows a different SLL and a different asymmetry present on the first side lobes of Fig. 15a. When steering the beam at 20 degrees, there is an aiming mismatch of 3 degrees between the traditional REV and the Selective-REV, which matches the measured active pattern. In contrast to the traditional approach, the selective method retrieves a pattern much closer to the real measurement. SLL imbalance and level are more accurate, especially in the steered beam configuration. The direction of the beam is within uncertainty compared to the measurement of the active pattern. The CCE encoding shows good agreement between the two measured encodings and the active pattern, as shown in Fig. 16. This behavior correlates with the simulation, where both encodings show very similar results. The comparative error between the Selective-REV and the CCE encodings is within the uncertainty of the measurement, so it is impossible to determine which result is more accurate than the real measurement.

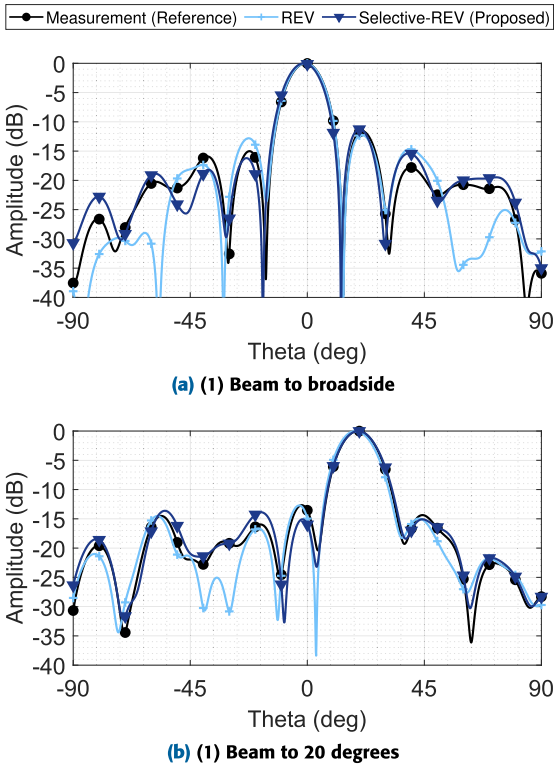

FIGURE 15. Comaprison between the measured diagram and the predicted using the REV methods.

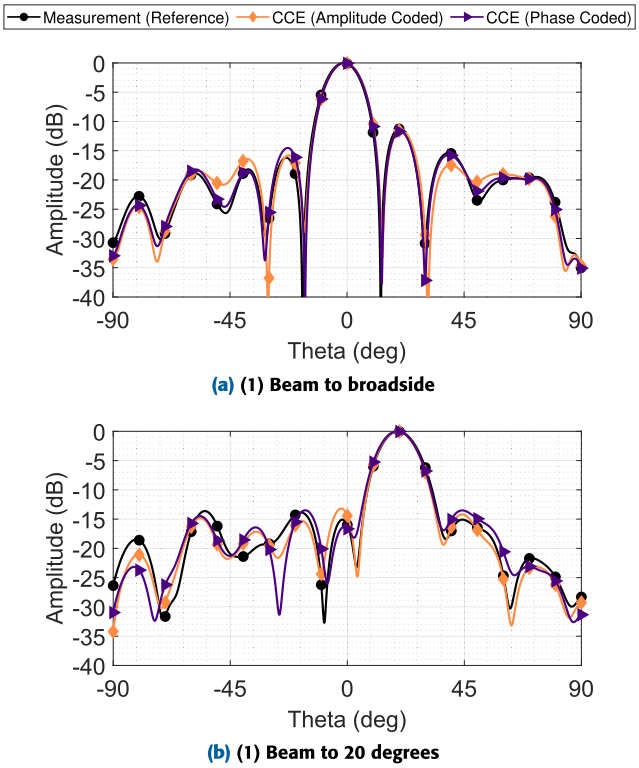

FIGURE 16. Comparison between the measured diagram and the predicted using amplitude or phase coded CCE.

B. PHASED ARRAY CALIBRATION

Attempting to directly correct the excitation of the phased array from the coefficient retrieved by the proposed Selective REV or CCE methods fails. As stated in Section II by Eq. 3, phase adjustment of a given channel significantly impacts the amplitude and phase of the adjacent ones. The amplitude adjustment of a channel has a minor impact on the adjacent channels since it only affects the coupling ratio. The characterization of this type of beamformer has shown that the induced phase change due to interchannel coupling is small (Fig. 3 and Fig. 4), so the relative phase adjustment can be interpreted as ideal. However, adjusting

the phase of a given channel significantly impacts that channel's amplitude, even for small phase changes. So, correcting both amplitude and phase simultaneously prevents the iterative approach from converging to the desired phased and amplitude distribution.

To overcome this limitation, the approach used for the phased array calibration is illustrated in Fig. 17. This approach consists of the following steps:

1) Retrieve the current excitation from the phased array using the proposed techniques.
2) Check if the phase distribution is within the desired tolerances. If not, adjust the phase difference between the desired and retrieved excitation. Return to the previous phase. A phase variation tolerance of ±10 degrees was set for the array under test.
3) When the phases are tolerable, correct the amplitude term as the difference between the desired amplitude factor and the retrieved one.
4) Calibration has been finished; if a lower phase or amplitude error is required, this process can be repeated to use more restrictive phase tolerances. This iteration loop can be helpful in calibrating small phased arrays operated with complicated beamforming techniques that are very sensible to excitation mismatches.

Two cases have been studied to verify this calibration approach using the same phased array system:

1) A defect in the manufacturing process of the phased array antenna induces huge static differences in the lengths of the distribution networks. The target excitation is a uniform amplitude excitation aiming to broadside.
2) A beamforming configuration with beam steering (to 20 deg) and nulling (at -30 deg) where the tolerances in phase and amplitude mismatches are reduced.

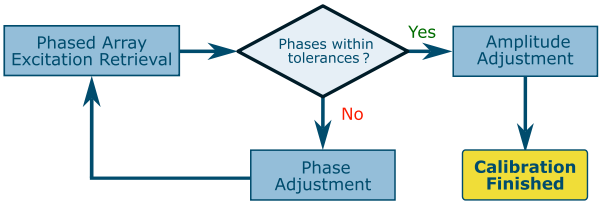

FIGURE 17. Iterative calibration procedure for the phased array system.

A deviation of ±10 deg from the desired phased array distribution has been set to calibrate the proposed configuration. The results achieved at each step of the calibration procedure are shown in Fig. 18. For the first configuration, the starting point is a phase mismatch of ±120 degrees and 3 dB in amplitude. This is the result of a poorly manufactured prototype. After an initial phase-only adjustment, the pattern is almost perfectly corrected. The amplitude correction effect is insignificant since it only equalizes the side lobes level

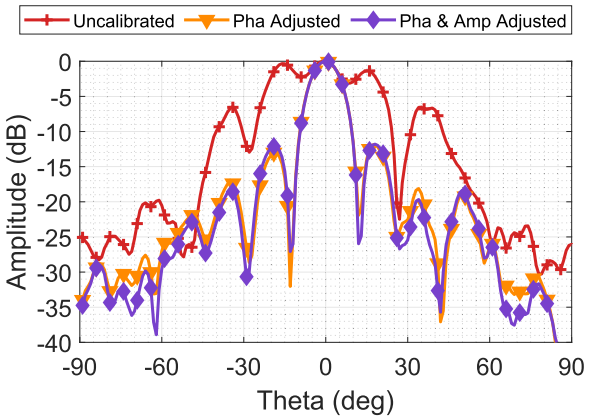

(a) Calibration for case 1.

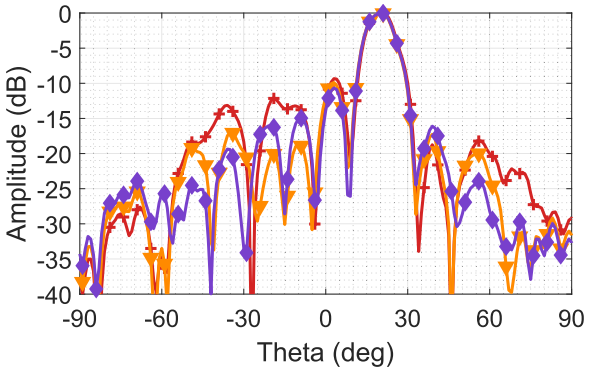

(b) Calibration for case 2.

FIGURE 18. Phased array patterns measured during the proposed calibration procedure.

for the first two lobes. For the second configuration, the initial excitation generates an exact aim of 20 degrees but misplaces the null by 3 degrees. The side lobes are also entirely distorted. After an iterative phase correction with three iterations, the shape of the side lobes is fixed, but the null is still misplaced. However, after correcting the amplitude mismatch, the null is finally placed at -30 degrees. For the first configuration, two iterations were needed for the phase adjustment. However, in the second case a third iteration was needed to match the stopping criteria perfectly.

These calibration procedures have been at a single frequency. As the phase and amplitude control stability over the frequency was ensured in [11], calibrating for a single frequency (usually the central frequency of the operating application) achieves a good broadband performance. The main concern with the single-frequency approach relies on the consistency of the coupling non-idealities. As depicted by Fig 5 over a 500 MHz bandwidth, the amplitude discrepancy is less than 0.7 dB in the worst-case scenario and its effect on the beamforming performance will be small.

V. CONCLUSION

This article shows an in-depth study of the non-idealities of commercial beamformers and their implications in the proce-

dures for phased array antenna excitation retrieval methods. The non-idealities of the beamformer have been modeled and tested with extensive S-Parameter measurements to acotate its effect on the excitation retrieval techniques. The two most popular peripheral probe calibration methods have been studied and adapted to the specificities of highly integrated phased-array antennas. This provides a good understanding of how these non-idealities introduce errors when decoding the phased array excitation from measurements. An adaptation to the active phased array scheme has been proposed for the REV method to reduce the error of the retrieved excitation coefficients. Through a simulation procedure that allows isolating of the measurement errors from the beamformer non-ideal behaviour, the array excitation retrieval methods have been analyzed, showing that the adapted Selective-REV method can improve the accuracy of the traditional approach, retrieving similar error results to the CCE encodings, which were the better performant methods. For the proposed small array, the accuracy of this method is within 1 dB in amplitude and 15 degrees in phase. The application of these methods for pattern prediction has been demonstrated with accurate and consistent results in both simulation and anechoic chamber measurements. Finally, the proposed iterative calibration procedure corrected the defects of a passive antenna. This calibration fixed the null's location and the sidelobes' shape in a beam-steered configuration.

ACKNOWLEDGMENT

The authors would like to express their sincere gratitude to Chengdu Xphased Technology Company Ltd., for generously lending them their products and evaluation boards, which were instrumental in the success of their project. They sincerely appreciate their exceptional support and guidance throughout the development of this work. Their commitment to excellent support and willingness to assist them at every research stage.

REFERENCES

[1] *5g Nr User Equipment (ue) Radio Transmission and Reception Part 2: Range 2 Standalone*, document TS 38.101-2, 3GPP, Sep. 2018.

[2] (Nov. 2018). *Highly Integrated Active Beam Forming Network for Ka-Band Phased Array Antennas (ARTES AT 5B.179)*. Accessed: Feb. 26, 2025. [Online]. Available: https://connectivity.esa.int/funding/highly-integrated-active-beam-forming-network-kaband-phased-array-antennas-artes-5b179

[3] *(N.D.) Ku Ka Dual Band Transmit Act Phased Array (ARTES AT 5B.236)*. Accessed: Feb. 26, 2025. [Online]. Available: https://esastar-publication-ext.sso.esa.int/ESATenderActions/details/75541

[4] Eur. Space Agency. *RF MEMS Based Ka Band Phased Array Antenna Prototype*. Accessed: Feb. 26, 2025. [Online]. Available: https://connectivity.esa.int/projects/RF-mems-based-ka-band-phased-array-antenna-prototype

[5] P. Shen, Y. Qi, W. Yu, F. Li, X. Wang, and X. Shen, "A directly connected OTA measurement for performance evaluation of 5G adaptive beamforming terminals," *IEEE Internet Things J.*, vol. 9, no. 16, pp. 15362–15371, Aug. 2022.

[6] K. Kibaroglu, M. Sayginer, T. Phelps, and G. M. Rebeiz, "A 64-element 28 GHz phased-array transceiver with 52 dBm EIRP and 8–12-Gb/s 5G link at 300 meters without any calibration," *IEEE Trans. Microw. Theory Techn.*, vol. 66, no. 12, pp. 5796–5811, Dec. 2018.

[7] A. Alammouri, J. Mo, V. V. Ratnam, B. L. Ng, R. W. Heath Jr., J. Lee, and J. Zhang, "Extending uplink coverage of mmWave and terahertz systems through joint phase-time arrays," *IEEE Access*, vol. 10, pp. 88872–88884, 2022.

[8] A. Gupta, U. Madhow, A. Arbabian, and A. Sadri, "Design of large effective apertures for millimeter wave systems using a sparse array of subarrays," *IEEE Trans. Signal Process.*, vol. 67, no. 24, pp. 6483–6497, Dec. 2019.

[9] S. Wyne, K. Haneda, S. Ranvier, F. Tufvesson, and A. F. Molisch, "Beamforming effects on measured mm-wave channel characteristics," *IEEE Trans. Wireless Commun.*, vol. 10, no. 11, pp. 3553–3559, Nov. 2011.

[10] F. Dai and J. Wu, "Efficient broadcasting in ad hoc wireless networks using directional antennas," *IEEE Trans. Parallel Distrib. Syst.*, vol. 17, no. 4, pp. 335–347, Apr. 2006.

[11] A. T. Muriel-Barrado, J. Calatayud-Maeso, A. Rodríguez-Gallego, P. Sánchez-Olivares, J. M. Fernández-González, and M. Sierra-Pérez, "Evaluation of a planar reconfigurable phased array antenna driven by a multi-channel beamforming module at ka band," *IEEE Access*, vol. 9, pp. 63752–63766, 2021.

[12] T. Yu and G. M. Rebeiz, "A 22–24 GHz 4-element CMOS phased array with on-chip coupling characterization," *IEEE J. Solid-State Circuits*, vol. 43, no. 9, pp. 2134–2143, Sep. 2008.

[13] N. Peng, P. Gu, and D. Zhao, "A Ka-band balanced four-beam phased-array receiver with symmetrical beam-distribution network in 65-nm CMOS," *IEEE Access*, vol. 9, pp. 110026–110038, 2021.

[14] L. Gao and G. M. Rebeiz, "A 22–44 GHz phased-array receive beamformer in 45 nm CMOS SOI for 5G applications with 3–3.6-dB NF," *IEEE Trans. Microw. Theory Techn.*, vol. 68, no. 11, pp. 4765–4774, Nov. 2020.

[15] S. Shakib, M. Elkholy, J. Dunworth, V. Aparin, and K. Entesari, "A wideband 28 GHz transmit-receive front-end for 5G handset phased arrays in 40-nm CMOS," *IEEE Trans. Microw. Theory Techn.*, vol. 67, no. 7, pp. 2946–2963, Jul. 2019.

[16] K.-J. Koh, J. W. May, and G. M. Rebeiz, "A millimeter-wave (40–45 GHz) 16-element phased-array transmitter in 0.18-μm SiGe BiCMOS technology," *IEEE J. Solid-State Circuits*, vol. 44, no. 5, pp. 1498–1509, May 2009.

[17] O. Inac, D. Shin, and G. M. Rebeiz, "A phased array RFIC with built-in self-test capabilities," *IEEE Trans. Microw. Theory Techn.*, vol. 60, no. 1, pp. 139–148, Jan. 2012.

[18] A. Katz, J. Wood, and D. Chokola, "The evolution of PA linearization: From classic feedforward and feedback through analog and digital predistortion," *IEEE Microw. Mag.*, vol. 17, no. 2, pp. 32–40, Feb. 2016.

[19] V. Åberg, H. Zhou, C. Fager, and L. Svensson, "RF PA predistortion using non-linear RF-DACs," in *Proc. IEEE Nordic Circuits Syst. Conf. (NorCAS)*, Oct. 2022, pp. 1–6.

[20] H. Huang, J. Xia, and S. Boumaiza, "Novel parallel-processing-based hardware implementation of baseband digital predistorters for linearizing wideband 5G transmitters," *IEEE Trans. Microw. Theory Techn.*, vol. 68, no. 9, pp. 4066–4076, Sep. 2020.

[21] H. M. Aumann, A. J. Fenn, and F. G. Willwerth, "Phased array antenna calibration and pattern prediction using mutual coupling measurements," *IEEE Trans. Antennas Propag.*, vol. 37, no. 7, pp. 844–850, Jul. 1989.

[22] C. Shipley and D. Woods, "Mutual coupling-based calibration of phased array antennas," in *Proc. IEEE Int. Conf. Phased Array Syst. Technol.*, Dana Point, CA, USA, Sep. 2000, pp. 529–532.

[23] D. Bekers, R. van Dijk, and F. van Vliet, "Mutual-coupling based phased-array calibration: A robust and versatile approach," in *Proc. IEEE Int. Symp. Phased Array Syst. Technol.*, Waltham, MA, USA, Oct. 2013, pp. 630–637.

[24] S.-C. Chae, H.-W. Jo, J.-I. Oh, G. Kim, and J.-W. Yu, "Coupler integrated microstrip patch linear phased array for self-calibration," *IEEE Antennas Wireless Propag. Lett.*, vol. 19, pp. 1615–1619, 2020.

[25] W. T. Patton and L. H. Yorinks, "Near-field alignment of phased-array antennas," *IEEE Trans. Antennas Propag.*, vol. 47, no. 3, pp. 584–591, Mar. 1999.

[26] S. Mano and T. Katagi, "A method for measuring amplitude and phase of each radiating element of a phased array antenna," *Electron. Commun. Jpn., Part I, Commun.*, vol. 65, no. 5, pp. 58–64, Jan. 1982.

[27] R. Long, J. Ouyang, F. Yang, W. Han, and L. Zhou, "Fast amplitude-only measurement method for phased array calibration," *IEEE Trans. Antennas Propag.*, vol. 65, no. 4, pp. 1815–1822, Apr. 2017.

[28] H.-J. Yoon and B.-W. Min, "Improved rotating-element electric-field vector method for fast far-field phased array calibration," *IEEE Trans. Antennas Propag.*, vol. 69, no. 11, pp. 8021–8026, Nov. 2021.

[29] R. Long, J. Ouyang, F. Yang, W. Han, and L. Zhou, "Multi-element phased array calibration method by solving linear equations," *IEEE Trans. Antennas Propag.*, vol. 65, no. 6, pp. 2931–2939, Jun. 2017.

[30] E. Lier, M. Zemlyansky, D. Purdy, and D. Farina, "Phased array calibration and characterization based on orthogonal coding: Theory and experimental validation," in *Proc. IEEE Int. Symp. Phased Array Syst. Technol.*, Waltham, MA, USA, Oct. 2010, pp. 271–278.

[31] R. Long, J. Ouyang, F. Yang, Y. Li, K. Zhang, and L. Zhou, "Calibration method of phased array based on near-field measurement system," in *Proc. IEEE Antennas Propag. Soc. Int. Symp. (APSURSI)*, Memphis, TN, USA, Jul. 2014, pp. 1161–1162.

[32] M. Li, F. Zhang, and W. Fan, "Fast array diagnosis based on measured complex array signals with short measurement distance," in *Proc. 16th Eur. Conf. Antennas Propag. (EuCAP)*, Madrid, Spain, Mar. 2022, pp. 1–5.

[33] S. Tang, Z. Wang, C. Pan, R. Su, W. Fan, and S. Gao, "A fast and efficient calibration method for phased array antennas using Fourier-structured excitation matrix," *IEEE Trans. Antennas Propag.*, vol. 71, no. 3, pp. 2290–2299, Mar. 2023.

[34] G. M. Rebeiz, S.-Y. Kim, O. Inac, W. Shin, O. Gurbuz, Y.-C. Ou, F. Golcuk, T. Kanar, and B.-H. Ku, "Millimeter-wave large-scale phased-arrays for 5G systems," in *IEEE MTT-S Int. Microw. Symp. Dig.*, Phoenix, AZ, USA, May 2015, pp. 1–3.

[35] H. Al-Saedi, W. M. Abdel-Wahab, S. M. Raeis-Zadeh, E. H. M. Alian, A. Palizban, A. Ehsandar, N. Ghafarian, G. Chen, S. Rasti Boroujeni, M.-R. Nezhad-Ahmadi, and S. Safavi-Naeini, "An integrated circularly polarized transmitter active phased-array antenna for emerging Ka-band satellite mobile terminals," *IEEE Trans. Antennas Propag.*, vol. 67, no. 8, pp. 5344–5352, Aug. 2019.

[36] K. K. Wei Low, A. Nafe, S. Zihir, T. Kanar, and G. M. Rebeiz, "A scalable circularly-polarized 256-element Ka-band phased-array SATCOM transmitter with ±60° beam scanning and 34.5 dBW EIRP," in *IEEE MTT-S Int. Microw. Symp. Dig.*, Boston, MA, USA, Jun. 2019, pp. 1064–1067.

[37] C.-Y. Kim, D.-W. Kang, and G. M. Rebeiz, "A 44–46 GHz 16-element SiGe BiCMOS high-linearity transmit/receive phased array," *IEEE Trans. Microw. Theory Techn.*, vol. 60, no. 3, pp. 730–742, Mar. 2012.

[38] Y. Yu, P. Baltus, and A. van Roermund, *Integrated 60 GHz RF Beamforming in CMOS*. Cham, Switzerland: Springer, 2011.

[39] M. A. Morton, J. P. Comeau, J. D. Cressler, M. Mitchell, and J. Papapolymerou, "Sources of phase error and design considerations for silicon-based monolithic high-pass/low-pass microwave phase shifters," *IEEE Trans. Microw. Theory Techn.*, vol. 54, no. 12, pp. 4032–4040, Dec. 2006.

[40] FCC. (2013). *FCC Report: SAT-LOI-20130319-00039*. Accessed: Dec. 3, 2024. [Online]. Available: https://fcc.report/IBFS/SAT-LOI-20130319-00039/990648.pdf

[41] N. Saponjic, F. Klefenz, F. Bongard, D. Llorens, A. Boulle, X. Aubry, A. Butler, F. Tiezzi, and S. Vaccaro, "Product concepts for land mobile satellite communication terminals in Ku-/Ka-band," in *Proc. 11th Eur. Conf. Antennas Propag. (EUCAP)*, Mar. 2017, pp. 1525–1529.

[42] W. Tadej and K. Życzkowski, "A concise guide to complex Hadamard matrices," *Open Syst. Inf. Dyn.*, vol. 13, no. 2, pp. 133–177, Jun. 2006.

[43] T. Takahashi, H. Miyashita, Y. Konishi, and S. Makino, "Theoretical study on measurement accuracy of rotating element electric field vector (REV) method," *Electron. Commun. Jpn., I, Commun.*, vol. 89, no. 1, pp. 22–33, Jan. 2006.

[44] M. D. Foegelle, "Fast simultaneous characterization of all analog phased array elements," in *IEEE MTT-S Int. Microw. Symp. Dig.*, Denver, CO, USA, Jun. 2022, pp. 859–861.

[45] Y. Aoki, Y. Hwang, S. Kim, Y. Kim, and S.-G. Yang, "Asynchronous 256-element phased-array calibration for 5G base station," *IEEE Microw. Wireless Compon. Lett.*, vol. 31, no. 6, pp. 798–801, Jun. 2021.

[46] J. E. Hansen, *Spherical Near-Field Antenna Measurements*. London, U.K.: Peter Peregrinus, 1988.

[47] C. F. Romero, A. Auñón Marugán, F. R. Varela, P. Bielza López, J. L. Alcolea Coronel, J. I. Alonso Montes, and M. S. Castañer, "EMF simulation of base station antennas in real sites using spherical wave expansion and diffracted fields," in *Proc. Antenna Meas. Techn. Assoc. Symp. (AMTA)*, Denver, CO, USA, Oct. 2022, pp. 1–5.

[48] D. M. Pozar, "The active element pattern," *IEEE Trans. Antennas Propag.*, vol. 42, no. 8, pp. 1176–1178, Aug. 1994.

[49] R. C. Hansen, *Frontmatter*. Hoboken, NJ, USA: Wiley, 2009. [Online]. Available: https://onlinelibrary.wiley.com/doi/abs/10.1002/9780470529188.fmatter

[50] T. B. Hansen and A. D. Yaghjian, *Plane Wave Theory of Time-Domain Fields, Near-Field Scanning Applications*. Piscataway, NJ, USA: IEEE Press, 1999.

[51] C. Cappellin, O. Breinbjerg, and A. Frandsen, "Properties of the transformation from the spherical wave expansion to the plane wave expansion," *Radio Sci.*, vol. 43, no. 1, pp. 1–16, Feb. 2008.

JORGE CALATAYUD MAESO (Graduate Student Member, IEEE) was born in Madrid, Spain, in 1997. He received the M.Sc. degree in telecommunication engineering from the Universidad Politécnica de Madrid (UPM), Spain, in 2021, where he is currently pursuing the Ph.D. degree. He is also a Research Assistant with the Grupo de Radiación (GR) Research Group, UPM. His research interests include control systems for RF applications, planar array antenna design, and the design of novel mm-wave antenna test ranges.

XIAOLIANG SUN was born in Shanghai, China. He received the B.Sc. degree in telecommunications engineering and the M.Sc. degree in signal theory and communications from the Universidad Politécnica de Madrid (UPM), Madrid, Spain, in 2016 and 2018, respectively. He is currently pursuing the Ph.D. degree in communications technologies and systems with UPM. Since 2016, he has been with the Radiation Group, Department of Signals, Systems, and Radiocommunications, UPM. His research interests include phased array antennas, smart antennas, and beam-forming networks in millimeter band.

ALFONSO TOMÁS MURIEL-BARRADO was born in Madrid, Spain, in 1990. He received the M.Sc. degree in telecommunication engineering from the Universidad Autónoma de Madrid (UAM), Spain, in 2015, and the Ph.D. degree from the Universidad Politécnica de Madrid (UPM), Spain, in 2023. In February 2020, he joined UAM, as an Adjunct Professor, where he currently holds the position of an Assistant Professor with the Group of Radio Frequency: Circuits, Antennas and Systems (RFCAS). He also collaborates intensively with the Grupo de Radiación (GR) Research Group, UPM. His current research interests include design and prototyping of new concepts of antenna arrays (passive, active, and reconfigurable) as well as the design and manufacture of microwave devices for SATCOM, SOTM, and 5G applications. Furthermore, he is also involved in antenna measurement field.

FERNANDO RODRIGUEZ VARELA was born in Ourense, Spain, in 1994. He received the M.Sc. and Ph.D. degrees in telecommunication engineering from the Technical University of Madrid, in 2018 and 2021, respectively. In 2019, he was a Visiting Scholar with the Technical University of Denmark. He was a Development Engineer with Huber+Suhner AG, from 2019 to 2021. Since 2022, he has been an Assistant Professor with Universidad Rey Juan Carlos, Madrid, Spain. He has authored a book chapter, three patent applications, 14 journal articles, and more than 30 international conferences. His current research interests include antenna design, measurements, and postprocessing techniques. In 2022, he was a recipient of the National Award of the Official College of Telecommunication Engineers of Spain for the Best Ph.D. Thesis, and in 2023, he received the Best Paper Award of the Antenna Measurement Techniques Association (AMTA) Symposium.

PABLO SÁNCHEZ-OLIVARES was born in Madrid, Spain. He received the M.Sc. and Ph.D. degrees in telecommunication engineering from the Universidad Autónoma de Madrid, Madrid, Spain, in 2011 and 2018, respectively. In 2019, he collaborated in research and development projects with the Universidad de Alcalá, and an Adjunct Professor with the Universidad Autónoma de Madrid. In September 2019, he joined the Escuela Técnica Superior de Ingenieros de Telecomunicación, Universidad Politécnica de Madrid, as an Assistant Professor. Since April 2022, he has been an Associate Professor with the Universidad Politécnica de Madrid. His current research interests include passive and active array antennas, including design and measurement.

JOSÉ-MANUEL FERNÁNDEZ-GONZÁLEZ (Senior Member, IEEE) was born in Lausanne, Switzerland. He received the Diplôme d'Ingénieur en Électricité degree from the École Polytechnique Fédérale de Lausanne, Lausanne, in 2003, and the Ph.D. degree from the Universidad Politécnica de Madrid, Madrid, Spain, in 2009. From 2006 to 2010, he got a FPU (national grant for teacher training) scholarship, as a Ph.D. Student with the Universidad Politécnica de Madrid. In 2006, he joined the Centre de Recherches Poly-Grames, École Polytechnique de Montréal, Montreal, QC, Canada, and in 2007, he joined the Chalmers University of Technology, Gothenburg, Sweden, as a Guest Ph.D. Student. From 2013 to 2019, he was an Assistant Professor with the Universidad Politécnica de Madrid. In 2018, he was a Fulbright Visiting Researcher with the Antenna Research Group, University of Colorado at Boulder. In 2019, he was an Associate Professor with the Universidad Politécnica de Madrid. He has authored more than 100 publications in scientific journals, symposium proceedings and seminars, three book chapters, and holds four patents. He has participated in more than 35 research projects and contracts. His current research interests include passive and active antennas, phased array antennas, RF circuits, and metamaterial structures. He is currently an Associate Editor of IEEE ANTENNAS AND WIRELESS PROPAGATION LETTERS.

MANUEL SIERRA CASTAÑER (Fellow, IEEE) was born in Zaragoza, Spain, in 1970. He received the degree in telecommunication engineering and the Ph.D. degree from the Technical University of Madrid (UPM), Spain, in 1994 and 2000, respectively. He has been with the Technical University of Madrid, as a Research Assistant and an Assistant, an Associate, and a Full Professor, since 1998. His current research interests include planar antennas and antenna measurement systems. He has been a member of the Board of Director of European Association of Antennas and Propagation, since 2016, where he is currently the Vice-Chair. He is an AMTA Fellow. He obtained the IEEE APS 2007 Schelkunoff Prize Paper Award for the paper "Dual-Polarization Dual-Coverage Reflectarray for Space Applications" in 2007.